Molten flux growth of single crystals of quasi-1D hexagonal chalcogenide BaTiS$_3$

Huandong Chen[1], Shantanu Singh[1], Hongyan Mei[2], Guodong Ren[3], Boyang Zhao[1], Mythili Surendran[1,4], Yan-Ting Wang[1], Rohan Mishra[5,3], Mikhail A. Kats[2,6], Jayakanth Ravichandran[1,4,7,a]

[1] Mork Family Department of Chemical Engineering and Materials Science, University of Southern California, Los Angeles, CA, USA
[2] Department of Electrical and Computer Engineering, University of Wisconsin-Madison, Madison, WI, USA
[3] Institute of Materials Science & Engineering, Washington University in St. Louis, St. Louis, MO, USA
[4] Core Center for Excellence in Nano Imaging, University of Southern California, Los Angeles, CA, USA
[5] Department of Mechanical Engineering and Materials Science, Washington University in St. Louis, St. Louis, MO, USA
[6] Department of Materials Science and Engineering, University of Wisconsin-Madison, Madison, WI, USA
[7] Ming Hsieh Department of Electrical and Computer Engineering, University of Southern California, Los Angeles, CA, USA
[a] Address all correspondence to this author. e-mail: j.ravichandran@usc.edu

Received: 1 April 2024; accepted: 17 June 2024

BaTiS$_3$, a quasi-1D complex chalcogenide, has gathered considerable scientific and technological interest due to its giant optical anisotropy and electronic phase transitions. However, the synthesis of high-quality BaTiS$_3$ crystals, particularly those featuring crystal sizes of millimeters or larger, remains a challenge. Here, we investigate the growth of BaTiS$_3$ crystals utilizing a molten salt flux of either potassium iodide, or a mixture of barium chloride and barium iodide. The crystals obtained through this method exhibit a substantial increase in volume compared to those synthesized via the chemical vapor transport method, while preserving their intrinsic optical and electronic properties. Our flux growth method provides a promising route toward the production of high-quality, large-scale single crystals of BaTiS$_3$, which will greatly facilitate advanced characterizations of BaTiS$_3$ and its practical applications that require large crystal dimensions. Additionally, our approach offers an alternative synthetic route for other emerging complex chalcogenides.

Introduction

Complex chalcogenides, highlighted by chalcogenide perovskites, have gathered considerable research interest recently due to their exciting electronic and optical properties [1–3]. Among them, the quasi-1D hexagonal chalcogenide, BaTiS$_3$, is a small bandgap semiconductor [2] that has shown pronounced optical anisotropy at mid-wave and long-wave infrared energies [2, 4], making it particularly attractive for polarization-selective infrared optics and optoelectronic devices [5–7], as revealed in Fig. 1(b) and (d). Furthermore, the recent discovery of charge density wave (CDW) electronic phase transitions [8] in single-crystalline BaTiS$_3$, along with the successful demonstration of neuronal device functionalities using this material [9], opens up compelling pathway for the development of electronic devices based on this novel phase-change material, as summarized in Fig. 1(c) and (e). However, despite the exciting physical

phenomena and the promising multifunctionality of BaTiS$_3$, its practical applications, especially for infrared optics, are largely limited by the attainable crystal sizes. For instance, the fabrication of BaTiS$_3$-based optical components, such as waveplates, necessitates crystals with well-defined optical axes and lateral dimensions of several millimeters or larger. Another compelling motivation for obtaining sizable and high-quality single crystals of BaTiS$_3$ arises from the urgent need of advanced characterization techniques, including neutron-based diffraction and scattering, to probe the underlying electronic phase transition mechanism. Many of these techniques require large crystal dimensions or volume [10, 11] for meaningful analysis.

To date, the synthesis of BaTiS$_3$ single crystals has exclusively relied on the iodine-assisted chemical vapor transport (CVT) method [2, 12], as illustrated in Fig. 2(a), where the size and morphology of crystals have certain limitations. For example, the quasi-1D BaTiS$_3$ crystals produced via this
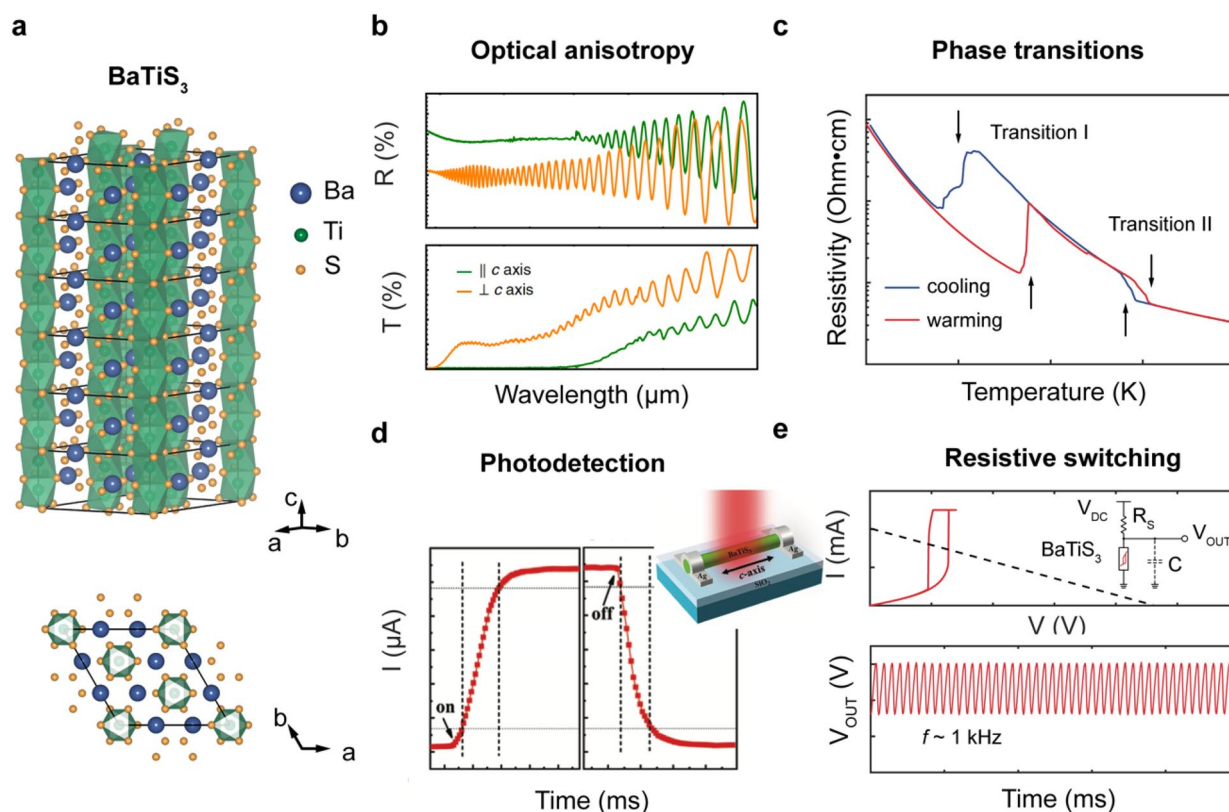
Figure 1: Intriguing physical properties and prototype device demonstrations of $BaTiS_3$. (a) Schematic illustration of quasi-1D $BaTiS_3$ crystal structure. Figure adapted from Ref. [8] (b) Polarized transmittance and reflectance of a $BaTiS_3$ crystal measured across the mid-infrared region (1.4 to 16 μm), showing large optical anisotropy. Figure adapted with permission from Ref. [6] (c) Temperature-dependent electrical resistivity of a $BaTiS_3$ crystal measured along the *c*-axis. The non-continuity and abrupt changes in resistivity indicate two phase transitions in $BaTiS_3$. Figure adapted from Ref. [8] (d) Transient photoresponse of a $BaTiS_3$ crystal. Figure adapted with permission from Ref. [12] (e) Threshold resistive switching and sustained voltage oscillations observed in a $BaTiS_3$ crystal. Figure adapted from Ref. [9].

method tend to form clusters of "thin needles" out of the powder due to the excessive number of nucleation sites (powder) during the growth process. Consequently, their dimensions perpendicular to the chain axis (both width and thickness) typically remain below 50 μm [12], as shown in Fig. 2(b). This is in stark contrast to the successful applications of CVT in producing various large-sized 2D transition metal dichalcogenide single crystals [13, 14]. An alternative and widely used synthesis technique is the high-temperature solution or molten flux growth method. This approach has been employed in obtaining various high-quality crystals with lateral dimensions of several millimeters or larger, benefiting from a well-controlled small number of nucleation sites and a slow cooling rate [15, 16]. As an example, millimeter-sized single crystals of the isostructural hexagonal chalcogenide $BaVS_3$ have already been obtained using either tellurium flux [17] or barium chloride flux [18]. Moreover, the development of flux growth can further advance other solution-based synthesis techniques such as solution Bridgeman, toward the realization of wafer-scale complex chalcogenide single crystals.

In this work, we present the first comprehensive study of single-crystalline $BaTiS_3$ growth via the flux method, using either potassium iodide (KI) or a mixture of barium chloride ($BaCl_2$) and barium iodide (BaI_2) as the salt flux. This KI flux approach yielded crystals of dimensions up to a centimeter in length and 500 μm in both width and thickness, while the $BaCl_2$-BaI_2 flux method produced thick (up to 200 μm) and plate-like $BaTiS_3$ crystals with (001)-orientation out-of-plane, both of which are significantly larger in volume compared to those synthesized through the conventional CVT technique [2, 19]. The high quality of the flux-grown crystals was validated through chemical and structural characterization conducted at room temperature. Optical anisotropy with a giant birefringence of up to 0.8 in the mid-infrared region and a substantial dichroic window from 1 to 4 μm were revealed in a flux-grown $BaTiS_3$ single crystal, through polarization-dependent infrared spectroscopy and ellipsometry analysis. Moreover, the electronic phase transitions were characterized by our combined temperature-dependent structural and transport measurements, the results of which are consistent with those observed in CVT-grown samples with
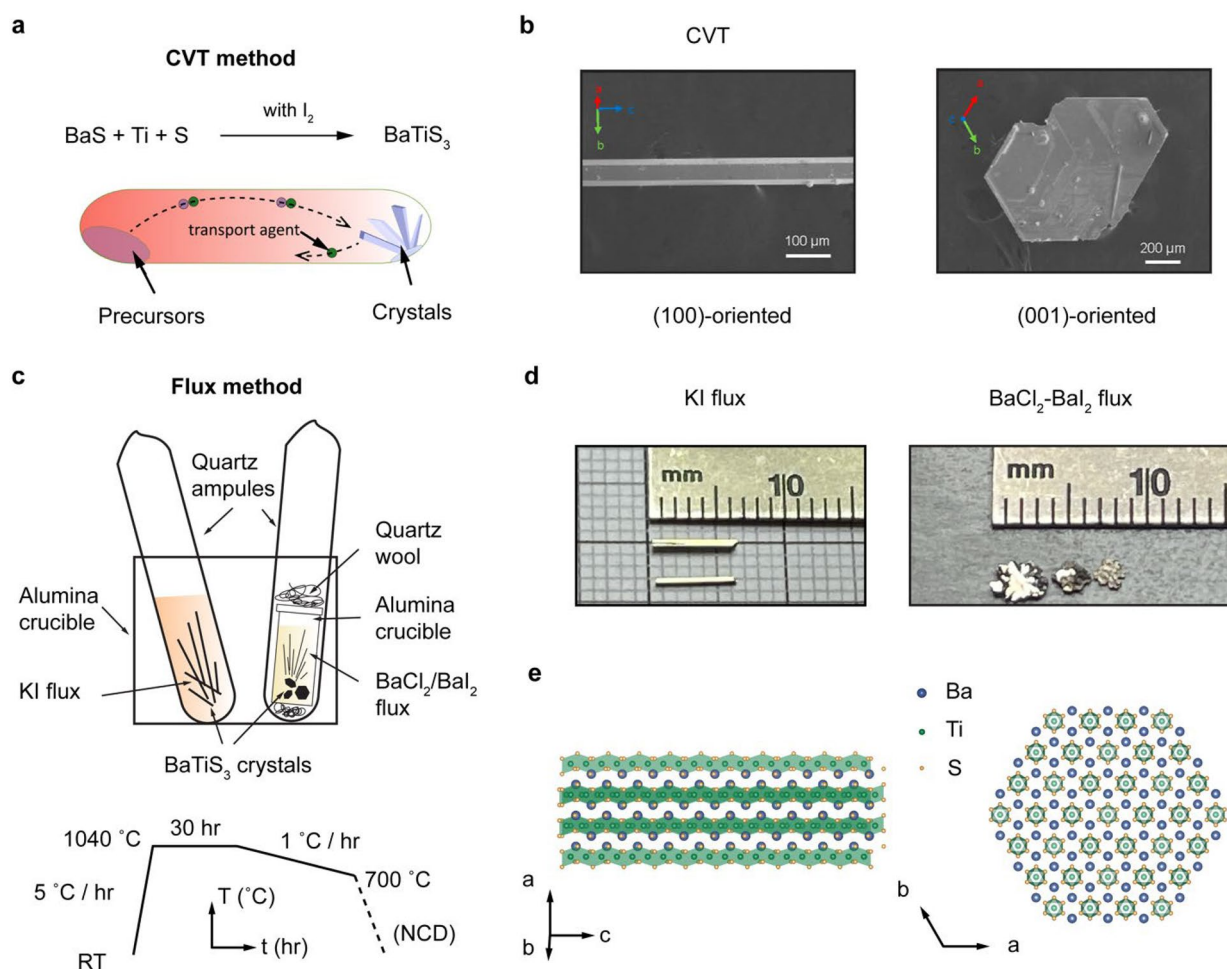
Figure 2: Growth methods of BaTiS$_3$ single crystals. (a) Schematic illustration of BaTiS$_3$ crystal growth from precursors using CVT method. The CVT schematic is adapted from Ref. [20] (b) Optical microscopic images of representative (100)- and (001)-oriented BaTiS$_3$ crystals grown by CVT method. Figure adapted with permission from Ref. [19], American Chemical Society. (c) Schematic illustration of molten flux growth of BaTiS$_3$ crystals using a vertical geometry (top) and the temperature profile used for the flux growth of BaTiS$_3$ (bottom). (d) Optical image of representative BaTiS$_3$ crystals grown with KI and BaCl$_2$-BaI$_2$ fluxes, respectively. KI flux growth yielded crystals with ~6 mm length and half a millimeter in both width and thickness. BaTiS$_3$ thick-plate-like crystals with 3 mm lateral dimensions and up to 250 µm thickness were obtained from BaCl$_2$-BaI$_2$ flux growth. (e) BaTiS$_3$ crystal structure viewed toward the *a-c* plane and along the *c*-axis.

a subtle shift in transition temperatures. Our study provides a feasible route for synthesizing high-quality, large BaTiS$_3$ single crystals using the flux growth method, which not only paves the way for practical device applications and advanced characterization of BaTiS$_3$, but also sheds light on the development of high-temperature solution-based synthesis of other complex chalcogenide materials.

Molten flux growth of BaTiS$_3$ crystals

Polycrystalline BaTiS$_3$ precursor powders were first prepared by conventional solid-state reaction at 1040 °C in a sealed quartz ampoule, and then the as-grown powders were annealed with excess sulfur pieces at 650 °C to heal the sulfur vacancies. Similar annealing process has been adopted to guarantee the sulfur

stoichiometry when synthesizing BaVS$_3$ crystals [21], whose magnetic properties are sensitive to sulfur vacancies. Single crystals of BaTiS$_3$ were grown using either KI or a BaCl$_2$-BaI$_2$ mixture as the molten flux, as illustrated in Fig. 2(c). For flux growth using KI, a mixture of the pre-synthesized BaTiS$_3$ powder, pre-dried KI powder (BaTiS$_3$: KI atomic ratio ~ 1:100), and sulfur pieces was placed directly in a sealed quartz ampoule; while for BaCl$_2$-BaI$_2$-based growth, a pre-mixture of BaCl$_2$ and BaI$_2$ was first loaded in a small aluminum crucible with the same BaTiS$_3$ powder (BaTiS$_3$: BaCl$_2$-BaI$_2$ mixture atomic ratio ~ 1:7) and excess sulfur , and then sealed in a straight quartz ampoule, in order to minimize the corrosion of quartz caused by BaCl$_2$.

The crystal growth procedures remain the same for both fluxes, where the mixture was first heated to 1040 °C to fully dissolve all the components and then slowly cooled to 700 °C

at a rate of 1 °C/h to allow the nucleation and continuous growth of $BaTiS_3$ crystals, after which the furnace was turned off for natural cooling, as illustrated in Fig. 2(c). After cooling down to room temperature, as-grown $BaTiS_3$ crystals were extracted by washing off excess salt flux using DI water. $BaTiS_3$ crystals obtained from KI flux growths typically feature lengths of several millimeters and both widths and thicknesses of up to 500 μm, whose dimensions perpendicular to the chain axis (along a- and b- axis) are substantially larger than those of CVT-grown crystals [12], as shown in the optical image [Fig. 2(d), left]. This dominant "thick needle-type" morphology of $BaTiS_3$ with hexagonal cross section is consistent with its quasi-1D crystal structure and a hexagonal symmetry, as illustrated in Fig. 2(e). Notably, a different "thick plate-like" crystal morphology with a- and b- axes in-plane (up to several millimeters laterally and 250 μm in thickness) was obtained from growths using $BaCl_2$-BaI_2 flux [Fig. 2(d), right], alongside with regular thin needle-like morphologies. Synthesis of such $BaTS_3$ crystals with c-axis out-of-plane has already been reported previously using the conventional CVT method [19]. However, the CVT-grown crystals have much smaller sizes, particularly in thickness.

The selection of either KI or $BaCl_2$-BaI_2 mixture as the flux material for $BaTiS_3$ growth in this work over many other halogen salts and metal fluxes was based on several important considerations as described below, in addition to its capability of dissolving $BaTiS_3$ powder at elevated temperatures. First, KI flux features a relatively low melting point of ~ 681 °C, which allows the growth to be performed at low temperatures [22] and enables a large process window for crystal nucleation and continuous growth. Similarly, the melting temperature of the $BaCl_2$-BaI_2 mixture is expected to be much reduced compared to pure $BaCl_2$ ($T_m \sim 962$ °C), due to the addition of the low melting temperature component BaI_2 ($T_m \sim 711$ °C). Second, compared to other commonly used halogen salts such as $BaCl_2$ [18, 23], KI is chemically less aggressive and does not require the use of doubly sealed quartz ampoules or special crucible materials such as alumina to protect the furnace and the furnace tubes. Hence, the overall growth process is significantly simplified. As for the $BaCl_2$-BaI_2 mixture, we applied an alumina crucible as the inner container and a second outer quartz sealing, in order to minimize the corrosion of quartz ampoule wall, which reduces the chance of leaking or explosion during the growth. Finally, unlike many metal fluxes that require high-temperature centrifuging process for crystal separation [15, 24], the excess KI or $BaCl_2$-BaI_2 salt can be easily removed by simply dissolving the salt in water at room temperatures due to their high solubility in water (~ 140 g KI/100 mL water, 35.8 g $BaCl_2$/100 mL water, and 221 g BaI_2/100 mL water,). The KI flux removal and crystal extraction steps are typically completed within one or two minutes, while for $BaCl_2$-BaI_2 mixture, these procedures usually take 10–15 min.

Room temperature chemical and structural characterization

Figure 3(a) illustrates a scanning electron microscopy (SEM) image of a representative KI flux-grown $BaTiS_3$ crystal that is about one order thicker than regular CVT-grown "thin" needles. Energy-dispersive X-ray spectroscopy (EDS) measurements were conducted on the crystal to assess its chemical composition. The mapping results, as depicted in the inset of Fig. 3(a), show a uniform distribution of Ba, Ti, and S elements throughout the field of view of the crystal. Figure 3(b) plots a representative EDS spectrum that quantifies a Ba: Ti: S atomic ratio of 1: 1.02: 2.96, suggesting a good stoichiometry. Noteworthily, no presence of either K or I element was observed within the detection limit of EDS with a standard deviation of 0.2% in atomic percentage, which indicates that the use of KI as a salt flux did not introduce a significant number of unintended elements in $BaTiS_3$ crystals during the growth.

A representative thin-film out-of-plane X-ray diffraction (XRD) scan of such crystals is shown in Fig. 3(c), where sharp 010-type reflections indicate the (010)-orientation of the crystal surface. We also performed polarization-resolved Raman spectroscopy on flux-grown $BaTiS_3$ crystals to reveal the anisotropic vibrational lattice properties [Fig. 3(d)]. Moreover, scanning transmission electron microscopy (STEM) studies were conducted to further confirm the quality of flux-grown $BaTiS_3$ crystals. An atomically resolved high-angle annular dark-field (HAADF) image of a $BaTiS_3$ crystal grown by KI flux, along the c-axis and its corresponding fast Fourier-transform (FFT), as shown in Fig. 3(e), clearly reveals the hexagonal arrangement of the Ba (the brightest columns) and Ti atomic columns (less bright columns). Additionally, electron energy loss (EEL) spectroscopy data were collected simultaneously for mapping the distribution of Ba, Ti, S, as illustrated in Figure S2.

Optical anisotropy

Optical anisotropy is one of the most exciting physical properties of $BaTiS_3$ crystals [2]. A giant broadband birefringence ($\Delta n = |n_e - n_o|$, where n_e and n_o are the extraordinary and ordinary refractive index, respectively) of up to 0.76 was reported in the mid- to long-wave infrared region in 2018 [6], which became a record at the time and is still among the highest in recently reported anisotropic optical crystals [25]. Moreover, two distinctive absorption edges at 0.28 eV and 0.78 eV were observed in CVT-grown $BaTiS_3$ crystals, leading to a large dichroic window in between [2].

We first evaluated the in-plane optical anisotropy of KI flux-grown $BaTiS_3$ crystals using polarization-resolved reflectance and transmittance using Fourier-transform
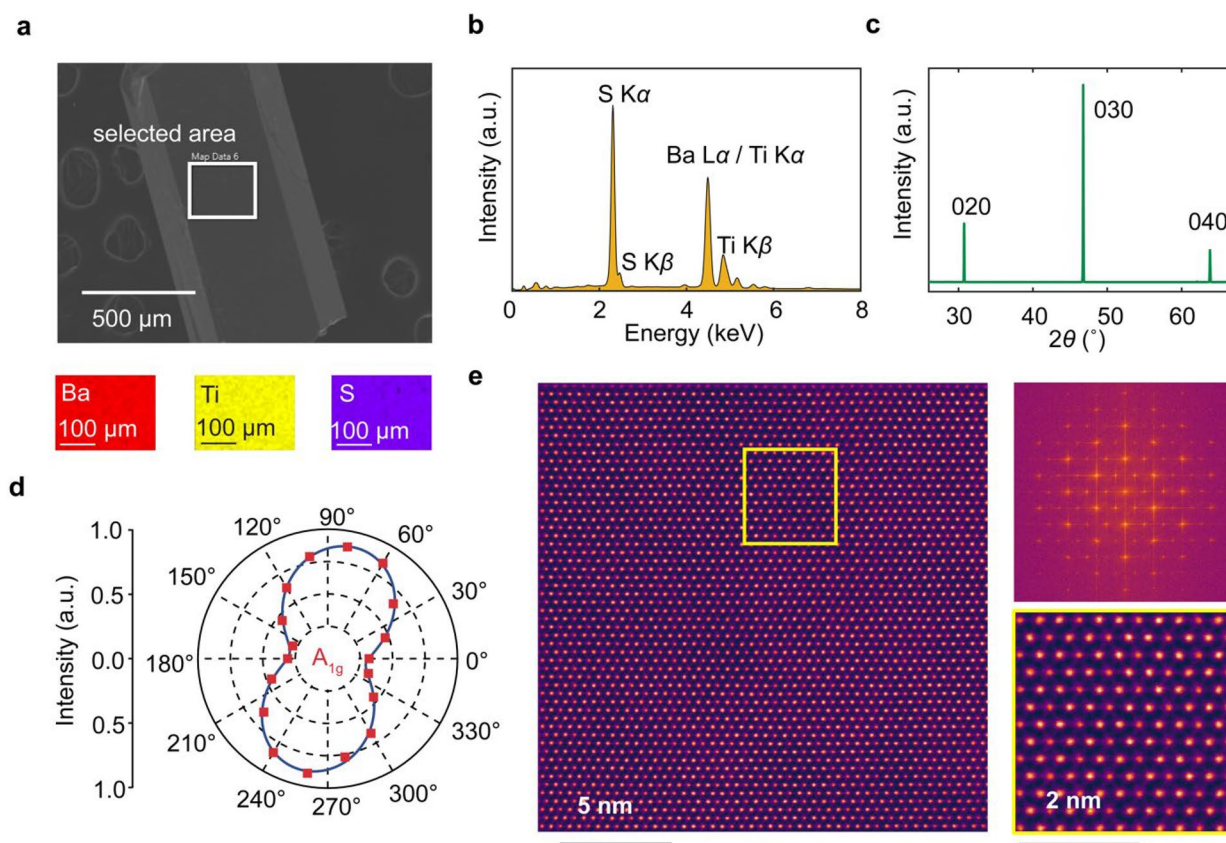
Figure 3: Room temperature, chemical, and structural characterization of flux-grown BaTiS$_3$. (a) SEM image of a representative thick BaTiS$_3$ crystal grown by KI flux. EDS mapping of barium (red), titanium (yellow), and sulfur (purple) elements in the selected area is shown as the inset. (b) EDS spectrum of flux-grown BaTiS$_3$ as in Fig. 2(a), showing Ba: Ti: S ratio as 1: 1.02: 2.96. (c) Out-of-plane XRD scan of a thick BaTiS$_3$ needle-like crystal grown by KI flux. (d) Intensity of A$_{1g}$ Raman mode of BaTiS$_3$ crystal at ∼ 380 cm^{-1} with different excitation laser polarizations plotted in polar coordinates. The blue line is the fitted curve. (e) Atomic resolution HAADF-STEM image of a KI flux-grown BaTiS$_3$ crystal viewed along the *c*-axis and the corresponding FFT pattern. Higher magnification HAADF-STEM image of BaTiS$_3$ acquired from the region highlighted with yellow box is illustrated at the bottom right.
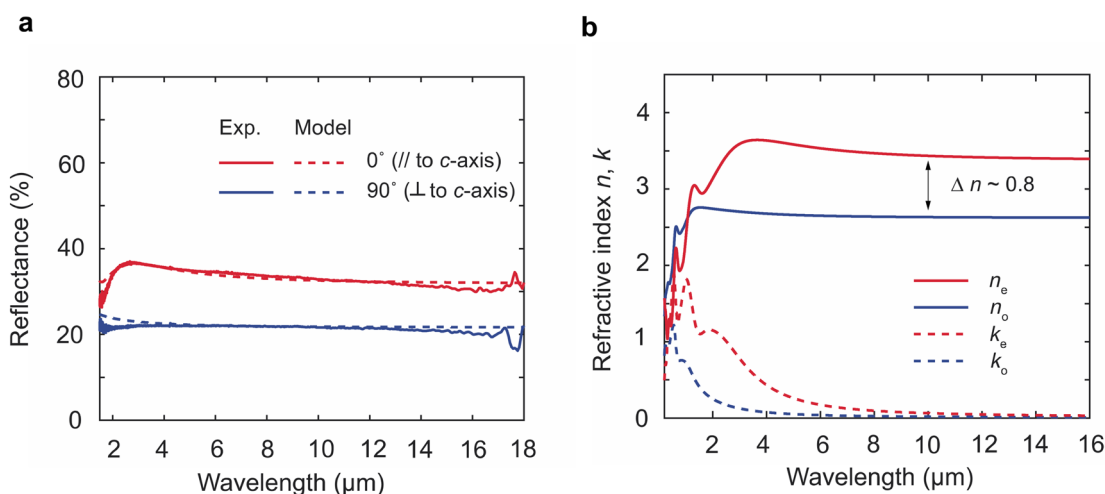

Figure 4: Optical anisotropy of flux-grown BaTiS$_3$. (a) Infrared reflectance spectra of a KI flux-grown BaTiS$_3$ crystal with incident light polarized at 0° and 90°, with respect to the *c*-axis. (b) Extracted complex refractive index values of flux-grown BaTiS$_3$ for the ordinary (perpendicular to *c*-axis) and extraordinary (parallel to *c*-axis) from visible to mid-infrared region.

infrared spectroscopy (FTIR). Figure 4(a) shows the reflectance spectra up to 18 μm that were collected with incident light polarized at 0° and 90° with respect to the *c*-axis, on a freestanding BaTiS$_3$ crystal with *a*- and *c*-axes in-plane (~ 250 μm thick). The large difference in the reflectance values between different polarizations clearly signifies that the flux-grown BaTiS$_3$ crystals are optically anisotropic similar to past reports [2, 19]. Unlike the optical spectra of thin platelets of BaTiS$_3$ crystals grown by the CVT method [2], the Fabry–Pérot fringes are absent from this measurement due to the substantial thickness of this flux-grown crystal.

To quantify the optical anisotropy, we extracted the complex refractive index for wavelengths from 210 nm to 16 μm by combining the FTIR measurements and spectroscopic ellipsometry measurements from 210 nm to 2.5 μm, following the analysis procedures reported elsewhere [2, 25]. Detailed fitting and analyses are presented in Methods and Supplementary Information. Figure 4(b) plots the corresponding dispersion of the real (*n*) and imaginary part (*κ*) of the refractive index for the ordinary (perpendicular to c-axis) and extraordinary (parallel to c-axis) directions. In the region with wavelengths of ~ 4 μm and above, the flux-grown BaTiS$_3$ shows a large birefringence of ~ 0.8, which is consistent with the reported values [2]. The model fits well for the reflectance spectra, as shown in Fig. 4(a).

However, the extracted dispersion of *κ* values may not be very accurate due to the absence of Fabry–Pérot fringes and the lack of information on absorption edges in the transmission spectra of thick samples (Figure S8). We determined the two absorption edges of flux-grown BaTiS$_3$ at ~ 0.35 and ~ 0.77 eV, respectively, from the transmission spectra of a thinner piece of crystal (~ 40 μm thick), which clearly reveals a large dichroic window and a slight shift of the low-energy edge, compared to reported values measured on CVT-grown crystals [2], as shown in Figure S9. The absence of substantial difference in transmittance spectra between different polarizations and the low absolute values of transmittance in thick flux-grown BaTiS$_3$ crystals (Figure S8) can be potentially attributed to the non-negligible scattering due to the defects in the crystals, misalignment of crystal optical axes or the use of an objective lens (NA of 0.17 and 0.4 in our measurements). Further improvements in the crystal quality, sizes, and the employment of large beam spot sizes during optical characterization shall be able to help resolve the issue. Nonetheless, the optical properties of flux-grown BaTiS$_3$ crystals are found to be largely consistent with those measured on CVT-grown samples [2], featuring both giant birefringence values in transparent regions and a large dichroism window.

Phase transitions

Besides its intriguing optical properties, BaTiS$_3$ has gained substantial research attention recently due to the discovery of electronic phase transitions [8] and the associated electronic functionalities [9] such as resistive switching. Several important questions concerning the underlying mechanism of phase transitions in such a semiconducting system were also raised [8]. An in-depth understanding of the CDW phenomena in BaTiS$_3$ necessitates experimental investigations into its phonon dispersion and electronic structure, using advanced techniques such as inelastic neutron scattering and angle-resolved photoemission spectroscopy. However, due to the limitations on the crystal dimensions of CVT-grown BaTiS$_3$ crystals, many of these techniques cannot be employed. Therefore, the flux growth method presented in this study, along with further growth optimizations, offers a promising route to overcome these limitations in characterizing BaTiS$_3$, toward unraveling the phase transition mechanism.

Here, we employed temperature-dependent structural and transport measurements to probe these phase transitions. Single-crystal XRD measurements were carried out on a BaTiS$_3$ crystal grown by KI flux at 100, 240, and 300 K, respectively, during the warming cycle, to reveal three different phases across the two phase transitions in BaTiS$_3$. Figure 5(a) to (c) shows the precession maps of flux-grown BaTiS$_3$ crystals projected onto the *hk*2 reciprocal plane at the corresponding temperatures, and Table S1 summarizes the evolution of unit cell sizes across the phase transitions, both of which agree well with previous reports of CVT-grown BaTiS$_3$ crystals [8]. Within the CDW phase, a series of weak superlattice reflections in diffraction patterns emerged compared to the room temperature structure, which is associated with a unit cell doubling in *a-b* plane across the charge density wave transition; while at 100 K, the superlattice peaks disappeared and the structure was completely distinctive from the room temperature phase. Similar results showing all three distinctive phases were observed in (001)-oriented BaTiS$_3$ crystals grown by the BaCl$_2$-BaI$_2$ flux, and the corresponding precession maps are illustrated in Figure S4.

Further, we conducted electrical transport measurements on a flux-grown BaTiS$_3$ to study the electronic phase transitions, as shown in Fig. 5(d). A relatively thin plate-like crystal (~ 50 μm thick) grown by BaCl$_2$-BaI$_2$ flux was intentionally selected for the ease of device fabrication, following the procedures reported elsewhere [8, 26]. Here, we identified transport anomalies with hysteresis windows at 175–200 K (Transition I) and 220–240 K (Transition II), respectively, which correspond to the two phase transitions reported in BaTiS$_3$. A slight shift of the Transition II (~ 20 K) toward the lower temperature and a reduced thermal hysteresis window of Transition I were observed in flux-grown BaTiS$_3$ crystals, compared to CVT-BaTiS$_3$ [8], despite the overall
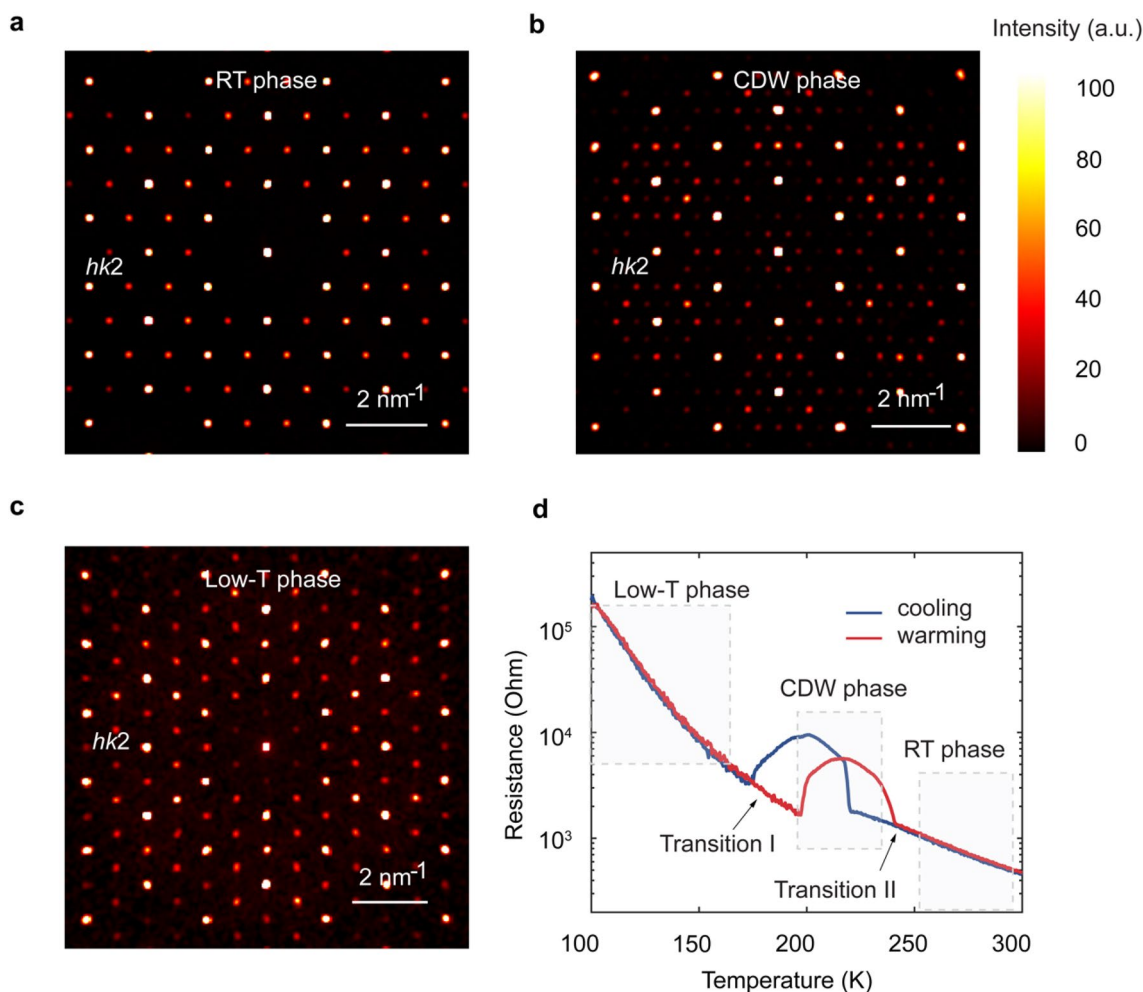
Figure 5: Phase transitions in flux-grown BaTiS$_3$. (a) to (c) Reciprocal precession images of flux-grown BaTiS$_3$ crystal along *hk*2 projection for three different phases. (d) Representative temperature-dependent electrical resistance of flux-grown BaTiS$_3$ crystal along the *c*-axis. Both the hysteretic phase transitions exist, consistent with CVT-BaTiS$_3$.

consistency in transport behavior. Although the origin of this discrepancy is not fully understood, we attribute it to the differences in the specific crystal growth conditions, considering the susceptibility of such phase transitions to a range of extrinsic factors such as strain [8] and potentially defects [27]. Nevertheless, this study is expected to promote in-depth investigations into the growth of large single crystals of complex chalcogenides, such as BaTiS$_3$, using flux growth and other techniques such as solution Bridgman growth method.

Conclusions

In conclusion, we have successfully synthesized large-scale single crystals of BaTiS$_3$ utilizing a molten flux method with either KI or BaCl$_2$-BaI$_2$ as the salt flux, from which the crystals grow an order of magnitude larger in sizes than those prepared using the conventional CVT approach. Importantly, this growth method

has preserved both the giant optical anisotropy and electronic phase transitions observed in crystals grown by vapor transport method. This confirms the high quality of these flux-grown BaTiS$_3$ crystals. Our study of flux growth of BaTiS$_3$ opens up new opportunities for its practical device applications in optics and optoelectronics, and it facilitates advanced material characterization toward a better understanding of these intriguing physical phenomena.

Moreover, we anticipate this flux-based crystal growth method, particularly with KI as the salt flux, would be broadly applicable for the synthesis of other emerging complex chalcogenide materials, such as highly anisotropic Sr$_{1+x}$TiS$_3$ that was recently reported to show a new record high birefringence of 2.1 [25] for optical applications and BaZrS$_3$ for potential photovoltaic applications [1, 28]. This method offers advantages over the utilization of highly corrosive BaCl$_2$ from various perspectives, as discussed in this manuscript. For BaCl$_2$-BaI$_2$ flux,

the reduced melting temperature of the flux mixture upon the addition of BaI_2 is also expected to favor the growth of large crystals. Nonetheless, it is important to note that unintended potassium doping, or iodine incorporation may pose challenges in certain specific material systems, which would need careful chemical analysis to clarify. Further, the successful demonstration of molten flux growth can enable more advanced growth techniques such as solution Bridgman growth, toward the synthesis of crystals with sizes that are suitable for neutron studies, or even as single-crystal chalcogenide wafers, which are important for in-depth material characterization and achieving high-quality epitaxial thin-film growth of complex chalcogenides in future.

Methods

Crystal synthesis

Polycrystalline $BaTiS_3$ powder was synthesized by first mixing a stoichiometric amount of barium sulfide powder (Sigma-Aldrich, 99.9%), titanium powder (Alfa Aesar, 99.9%), with a 5% excess of sulfur (Sigma-Aldrich, 99.998%). The mixture was loaded into a sealed, evacuated quartz ampoule and heated to 1040 °C at a rate of 50 °C/h. The ampoule was cooked for 160 h and then quenched in NaCl/ice bath. The resulting material is in the form of loosely packed black powder. The obtained $BaTiS_3$ powder was then loaded into another quartz ampoule with sulfur pieces ($BaTiS_3$: S weight ratio ~ 2:1) for sulfur annealing. The ampoule was cooked at 650 °C for 80 h in a tube furnace. The excess sulfur was separated from $BaTiS_3$ powder by re-heating the mixture such at sulfur could condense at the cold end.

For single-crystal growth using KI, 10 g pre-dried KI powder (Alfa Aesar, 99.9%) and 200 mg pre-synthesized $BaTiS_3$ powder ($BaTiS_3$:KI atomic ratio ~ 1:100) were placed in a quartz ampoule with 19 mm of outer diameter (OD), 2 mm of wall thickness, and approximately 8 cm in length, mixed with and 10 mg excess S powder in a N_2-filled glovebox. The ampoule was then sealed under vacuum. It is important to dry the as-purchased KI powder in glovebox at 110 °C overnight before using, in order to avoid explosion at high temperatures. For $BaTiS_3$ crystal growth using $BaCl_2$-BaI_2 mixture, 0.5 $BaCl_2$ powder (Alfa Aesar, 99.998%), 1.5 g BaI_2 powder (Alfa Aesar, 99.999%), and 50 mg pre-synthesized $BaTiS_3$ powder were thoroughly mixed and placed in a small aluminum crucible (Canfield crucible set, 2 mL), before loading into a straight quartz ampoule (15 mm inner diameter (ID), 19 mm OD, ~ 20 cm long). Quartz wool was used to fix the aluminum crucible position and a small quartz cap (10 mm ID, 14 mm OD, ~ 3 cm long) was used to seal the ampoule. Figure S5 shows an optical image of a sealed ampoule for BaCl2-BaI2 flux growth.

After sealing, the quartz ampoules were placed in an alumina crucible and then loaded into a box furnace (modified from a 6-inch three zone tube furnace) with a vertical configuration as illustrated in Fig. 1(a). The ampoules were heated to 1040 °C in 30 h and hold at 1040 °C for 30 h, followed by a slow cooling step to 700 °C at 1 °C/h before a natural cooling down process [Fig. 1(c)]. After about 20 days, the ampoule was removed from the furnace and washed with DI water to remove the excess salt. Crystals were picked individually after drying under an optical stereo microscope for further characterizations. Figure S6 illustrates the optical images of several different $BaTiS_3$ crystal synthesis steps using KI flux.

Chemical, vibrational, and electron microscopic characterization

Energy-dispersive X-ray spectroscopy (EDS) was performed using UltimMax 170 spectrometer attached on a NanoSEM 450 system. Polarization-dependent Raman spectroscopy was performed in a backscattering geometry using a conformal microscopic spectrometer. The incident beam (532 nm) was linearly polarized, and a half-wave plate was used for polarization rotation.

Scanning transmission electron microscopy (STEM) imaging was performed using an aberration corrected Nion UltraSTEM 100 (operated at 100 kV) microscope at Oak Ridge National Laboratory. HAADF-STEM images were acquired using a convergence semi-angle of 30 mrad and an annular dark-field detector with inner and outer collection semi-angles of 80 and 200 mrad, respectively. EELS was carried out using a Gatan Enfina EEL spectrometer attached to the Nion UltraSTEM. A collection semi-angle of 48 mrad and an energy dispersion of 1 eV per channel were used to acquire EELS data.

Infrared spectroscopy and ellipsometry

Polarization-resolved infrared spectroscopy was conducted using a Fourier-transform infrared spectrometer (Bruker Optics Vertex 70) and an infrared microscope (Hyperion 2000). A 15 × Cassegrain microscope objective (NA = 0.4) was used for both transmittance and reflectance measurements at near-normal incidence on a (100) face of a KI-grown $BaTiS_3$ crystal. The polarization of incident light was controlled using a wire-grid polarizer. The measurements were performed using a Globar source, a potassium bromide beam splitter and a mercury cadmium telluride detector.

Ellipsometry measurements were carried out using a VASE ellipsometer (J. A. Woollam Co.) with focusing probes over a spectral range of 210 nm to 2.5 μm at an angle of incidence of 55°. Data were acquired from three different sample orientations (optical axis parallel, perpendicular, and ~ 48° to the plane of incidence). Data analysis and refractive index extraction were

performed using WVASE software (J. A. Woollam Co.). See more details in the Supplementary Note 1.

X-ray diffraction

The single-crystal X-ray diffraction measurements were carried out on a Rigaku XtaLAB Synergy-S diffractometer at University of Southern California. Crystals were mounted on MiTeGen Dual Thickness MicroMounts™ and placed in a nitrogen cold stream on the goniometer-head of the diffractometer, which is equipped with a Mo K α X-ray source (wavelength 0.71 Å) and a HyPix-6000HE detector. Diffraction data were collected ensuring at least 99.9% completeness for a resolution of 0.70 Å. Data reduction, scaling, unit cell determination, and precession map analysis were done in CrysAlisPro.

The thin-film out-of-plane XRD scan was performed in a Bruker D8 Advance diffractometer using a Ge (004) two bounce monochromator with Cu $K_{\alpha 1}$ radiation at room temperature.

Device fabrication and transport measurements

Flux-grown $BaTiS_3$ crystal was first embedded in a polyimide medium for planarization [26] and then regular photolithography and ebeam evaporation were applied to form electrodes, following the procedures reported elsewhere. Standard low-frequency ($f = 17$ Hz) AC lock-in techniques were used to measure sample resistance in four-probe geometry from 100 to 300 K, with an excitation current of about 100 nA.

Author contributions

H.C. conceived the idea and designed the experiments. J.R. supervised the project. H.C. grew the crystals, fabricated devices, and performed the transport measurements. S.S., H.C, and M. S. carried out the chemical analysis. S.S., H.C., and B.Z. conducted XRD measurements and analysis. G.R. performed the STEM studies under the supervision of R.M. H.M. carried out infrared spectroscopy and ellipsometry measurements under the supervision of M.K. H.C. and J.R. wrote the manuscript with input from all other authors.

Data availability

The data are available from the corresponding author of the article on reasonable request.

Declarations

Conflict of interest The authors declare no competing financial interests.

Supplementary Information

The online version contains supplementary material available at https://doi.org/10.1557/s43578-024-01379-5.

Open Access

References

1. Y.-Y. Sun, M.L. Agiorgousis, P. Zhang, S. Zhang, Chalcogenide perovskites for photovoltaics. Nano Lett. **15**, 581–585 (2015)

2. S. Niu et al., Giant optical anisotropy in a quasi-one-dimensional crystal. Nat. Photonics **12**, 392–396 (2018)

3. S. Niu et al., Bandgap control via structural and chemical tuning of transition metal perovskite chalcogenides. Adv. Mater. **29**, 1604733 (2017)

4. J. Wu et al., Linear dichroism conversion in quasi-1D perovskite chalcogenide. Adv. Mater. **31**, 1902118 (2019)

5. S. Huang et al., In-plane optical anisotropy of layered gallium telluride. ACS Nano **10**, 8964–8972 (2016)

6. G. Ermolaev et al., Giant optical anisotropy in transition metal dichalcogenides for next-generation photonics. Nat. Commun. **12**, 854 (2021)

7. L. Tong et al., Stable mid-infrared polarization imaging based on quasi-2D tellurium at room temperature. Nat. Commun. **11**, 2308 (2020)

8. H. Chen et al., Charge density wave order and electronic phase transitions in a dilute d-band semiconductor. Adv. Mater. **35**, 2303283 (2023)

9. H. Chen et al., Charge-density-wave resistive switching and voltage oscillations in ternary chalcogenide BaTiS$_3$. Adv. Electron. Mater. **9**, 2300461 (2023)

10. J. Rossat-Mignod et al., Inelastic neutron scattering study of cerium heavy fermion compounds. J. Magn. Magn. Mater. **76**, 376–384 (1988)

11. J. Axe, G. Shirane, Inelastic-neutron-scattering study of acoustic phonons in Nb$_3$Sn. Phys. Rev. B **8**, 1965 (1973)

12. F. Yang et al., Strongly anisotropic quasi-1D BaTiS$_3$ chalcogenide perovskite for near-infrared polarized photodetection. Adv. Optic. Mater. **11**, 2201859 (2022)

13. A. Thompson, R. Gamble, J. Revelli, Transitions between semiconducting and metallic phases in 1-T TaS$_2$. Solid State Commun. **9**, 981–985 (1971)

14. J.A. Wilson, A. Yoffe, The transition metal dichalcogenides discussion and interpretation of the observed optical, electrical and structural properties. Adv. Phys. **18**, 193–335 (1969)

15. P.C. Canfield, Z. Fisk, Growth of single crystals from metallic fluxes. Philos. Mag. B **65**, 1117–1123 (1992)

16. V.V. Klepov, C.A. Juillerat, K.A. Pace, G. Morrison, H.-C. Zur Loye, "Soft" alkali bromide and iodide fluxes for crystal growth. Front. Chem. **8**, 518 (2020)

17. H. Kuriyaki et al., Synthesis and characterization of BaVS$_3$ single crystals grown in melted Te. Synth. Met. **71**, 2049–2050 (1995)

18. R. Gardner, M. Vlasse, A. Wold, Preparation, properties and crystal structure of barium vanadium sulfide, BaVS$_3$. Acta Crystallogr. Sect. B: Struct. Crystallogr. Cryst. Chem. **25**, 781–787 (1969)

19. B. Zhao et al., Orientation-controlled anisotropy in single crystals of quasi-1D BaTiS$_3$. Chem. Mater. **34**, 5680–5689 (2022)

20. A.F. May, J. Yan, M.A. McGuire, A practical guide for crystal growth of van der Waals layered materials. J. Appl. Phys. (2020)

21. O. Massenet et al., BaVS$_3$, a quasi-one dimensional ferromagnet or antiferromagnet depending on stoichiometry. Mater. Res. Bull. **13**, 187–195 (1978)

22. M. Tachibana, *Beginner's Guide to Flux Crystal Growth* (Springer, 2017)

23. S. Niu et al., Crystal growth and structural analysis of perovskite chalcogenide BaZrS$_3$ and Ruddlesden-Popper phase Ba$_3$Zr$_2$S$_7$. J. Mater. Res. **34**, 3819–3826 (2019)

24. N. Ni et al., First-order structural phase transition in CaFe$_2$As$_2$. Phys. Rev. B **78**, 014523 (2008)

25. H. Mei et al., Colossal optical anisotropy from atomic-scale modulations. Adv. Mater. **35**, 2303588 (2023)

26. H. Chen, A. Avishai, M. Surendran, J. Ravichandran, A polymeric planarization strategy for versatile multiterminal electrical transport studies on small, bulk crystals. ACS Appl. Electron. Mater. **4**, 5550–5557 (2022)

27. H. Imai, H. Wada, M. Shiga, Calorimetric study on metal-insulator transition of quasi-one-dimensional BaVS$_3$. J. Phys. Soc. Jpn. **65**, 3460–3463 (1996)

28. M. Surendran et al., Epitaxial thin films of a chalcogenide perovskite. Chem. Mater. **33**, 7457–7464 (2021)